Insights on the capabilities and improvement ability of classical many-body potentials: Application to α -zirconium

Alessandra del Masto, Jean Baccou, Guy Tréglia, Fabienne Ribeiro, Céline Varvenne

Insights on the capabilities and improvement ability of classical many-body potentials: application to α-zirconium

Alessandra Del Masto[a,b,*], Jean Baccou[a], Guy Tréglia[b], Fabienne Ribeiro[a], Céline Varvenne[b,*]

[a] *Institut de Radioprotection et de Sureté Nucléaire (IRSN), PSN-RES/SEMIA/LSMA, St Paul-Lez-Durance, France.*
[b] *Aix Marseille Univ., CNRS, CINaM, Marseille, France*

Abstract

Classical many-body potentials that have a rather low number of parameters and are based on physically-inspired functional forms are expected to display a reasonable transferability, though their flexibility is limited. Ways to improve them when their transferability is unsatisfactory and when new interesting structures/targeted properties emerge are not clearly established. Here, model screening and sensitivity analysis techniques are combined to get insights on the intrinsic capabilities of classical potentials for typical sets of targeted properties, and we propose to use the outcomes of the sensitivity analysis to improve potential performances. Usefulness is illustrated on existing simple second moment potentials (SMA), and we refit one such model for the study of small irradiation defects in α-zirconium. Application of this approach is recommended for more complex interaction models with up to tens of parameters, such as other classical many-body potentials or tight-binding electronic structure models, that are possible to re-optimize while gaining a better understanding of the role of their parameters.

Keywords: Classical interatomic potentials, Sensitivity analysis, atomistic calculations, α-zirconium, irradiation defects

1. Introduction

Classical many-body potentials having low to intermediate number of parameters are based on a physical understanding of the interatomic bonding, which makes them reasonably transferable [1]. They have been extensively used up to now to uncover mechanisms occuring at large scales [2–5], to investigate complex defect diffusion and potential energy landscapes [6, 7], to assist the development of mesoscale models of materials properties [8, 9], or to perform full phase diagram calculations of multicomponent bulk alloys or nano-objects [10, 11]. None of these results could have been obtained from *ab initio* atomistic calculations: the large space and time scales accessible to classical interatomic potentials are a prerequisite to undertake such studies.

More recently, another class of interatomic potentials – the so-called Machine Learning (ML) potentials – has become very popular in the materials science community [12–14]. In contrast to classical potentials, ML potentials have a very high dimensionality in the parameter space [1, 15–17]. This gives them a high flexibility, and thus very good interpolation capabilities. Their transferability/extrapolation behavior on the other hand depends on the subclass of ML potentials [1, 13]. However, their development requires a very large *ab initio* database of structures, energies and forces, and the numerical cost associated with their use remains several orders of magnitude higher than those of classical potentials [1, 18]. This places ML potentials in between *ab initio* methods and classical potentials in the multi-scale modeling chain.

Consequently, some classes of physical problems can only be treated by classical, numerically light potentials, *e.g.* embedded-atom-method (EAM) [19, 20], tight-binding second moment approximation (SMA) [21], or modified EAM potentials [22, 23]; so one must continue to develop and improve them for materials studies, knowing that their flexibility is limited. The identification of potential parameters for a specific system and set of targeted properties thus remains a critical step, and calls for a better understanding of the actual capabilities of a given potential-type to reproduce some properties or combination of properties. Moore *et al.* [24] tackled this problem using qualitative, one-at-a-time sampling of the MEAM potential parameters, and provided useful insights into how changes in parameters propagate on several structural and thermal material properties. However, such an approach ignores the possible sensitivity of the interatomic potential to the correlation between its parameters. No work has been carried out to date that takes these effects into account in a quantitative and systematic manner, and that deals with typical realistic sets of target simulated properties (*e.g.* including defects). Indeed, the current literature is either devoted to the study of fcc bulk properties [25], and/or

*Corresponding author
Email addresses: alessandra.delmasto@irsn.fr (Alessandra Del Masto), celine.varvenne@cnrs.fr (Céline Varvenne)

focused on the quantification of uncertainties [25–27].

In this work, we perform an analysis based on model screening and variance-based global sensitivity analysis tools to get insights on the above-mentioned aspects, and propose to use the outcomes of the sensitivity analysis to improve existing potentials. The interest and usefulness of this approach is illustrated on the model case of SMA potentials – simple many-body potentials having a very low number of parameters – and examined in the context of irradiation defects in α-zirconium. But the approach is general, and also applies to other classical potentials.

The remainder of the article is organized as follows. Section 2 introduces the SMA interaction model and the selected bulk and defect quantities of interest for α-Zr. Model screening is performed in section 3, and allows us to identify (i) some difficulties of the SMA to describe several defect properties, and (ii) the possible artifacts induced by the existence of strong gradient zones in the potential functions. After reduction of these artefacts, the most influential parameters on each of the computed properties are identified in section 4, through a variance-based sensitivity analysis. Section 5 illustrates the refitting process of an existing potential, focusing on a reduced number of important parameters. Interesting insights on the actual capabilities of SMA potentials for reproducing the set of selected α-Zr properties are obtained, and an existing SMA potential is improved for the study of small point defect physics. Section 6 is dedicated to various discussions about the SMA capabilities, the interest of our combined approach, and its applicability to other types of interaction models.

2. Atomistic simulation details

We first describe the functional form and parameter sets of the SMA potentials, and then list the quantities of interest for studying irradiation defects in hcp Zr, a major component of the nuclear cladding materials.

2.1. Second Moment Approximation (SMA) potentials

The second-moment approximation of the tight-binding scheme (TB-SMA) proposed by Rosato *et al.* [21], and following the ideas of Friedel and Ducastelle [28–31], provides an analytical form for the energy of a particle and a particle assembly [21, 32, 33]. This family of classical interatomic potentials has been designed for transition metals. With this formalism, the energy of an atomic site i, with $i = 1...N_{\rm at}$ for a system of $N_{\rm at}$ atoms, is written as:

$$E_i^{\rm tot} = E_i^{\rm b} + E_i^{\rm rep}, \tag{1}$$

with $E_i^{\rm b}$ the band energy term, attractive, and $E_i^{\rm rep}$ the empirical repulsive term. The band term is derived from a simplified electronic structure of the metal and has the following form:

$$E_i^{\rm b} = -\xi \sqrt{\sum_{j\neq i} e^{-2q\left(\frac{r_{ij}}{r_0}-1\right)}}, \tag{2}$$

where r_0 represents a typical distance, close to the first nearest neighbor atoms, and r_{ij} is the distance between atoms located at sites i and j. $\xi > 0$ is an effective hopping integral, and q describes the interatomic distance dependence. Interactions are non-additive due to the presence of the square root in Eq. 2. The repulsive interaction term is assumed to be pairwise and described by a sum of Born-Mayer ion-ion repulsion terms:

$$E_i^{\rm rep} = A \sum_{j\neq i} e^{-p\left(\frac{r_{ij}}{r_0}-1\right)}, \tag{3}$$

where $A > 0$ provides the energy scale, and p sets the decay. The total potential energy of the system is then expressed as $E^{\rm tot} = \sum_{i=1}^{N_{\rm at}} E_i^{\rm tot}$. Note that original formulations of EAM and Finnis-Sinclair potentials were very close to the SMA one.

To limit summations in Eqs. 2 and 3, a cutoff radius $r_{\rm cut}$ must be chosen, and defines the range of the SMA potential. It typically falls between two successive atomic neighbor shells in the bulk crystalline structure (here hcp) [32]. Numerically, this cutoff is defined as an interval $r_{\rm cut} \equiv [r_{\rm cut}^{\rm s}, r_{\rm cut}^{\rm e}]$, which extremities correspond to the starting and ending points of a polynomial function smoothly linking the energy to zero. Thus, the energy of an atomic site i for distances larger than $r_{\rm cut}^{\rm s}$ is computed as:

$$E_i^{\rm tot} = \sum_{j\neq i} \alpha(r_{ij}) - \sqrt{\sum_{j\neq i} \Xi^2(r_{ij})}, \tag{4}$$

with $r_{\rm cut}^{\rm s} < r_{ij} < r_{\rm cut}^{\rm e}$, and where

$$\begin{aligned}\alpha(r_{ij}) &= a_3(r_{ij}-r_{\rm cut}^{\rm e})^3 + a_4(r_{ij}-r_{\rm cut}^{\rm e})^4 + a_5(r_{ij}-r_{\rm cut}^{\rm e})^5,\\ \Xi(r_{ij}) &= x_3(r_{ij}-r_{\rm cut}^{\rm e})^3 + x_4(r_{ij}-r_{\rm cut}^{\rm e})^4 + x_5(r_{ij}-r_{\rm cut}^{\rm e})^5.\end{aligned} \tag{5}$$

This SMA potential formulation is implemented in the open source molecular dynamics (MD) software LAMMPS [34], and the six coefficients $(a_3, a_4, a_5, x_3, x_4, x_5)$ of the polynomial functions are automatically computed, from continuity conditions applied between the exponentials of Eqs. 2 and 3 and the polynomials of Eqs. 5, up to their second derivatives. An SMA potential developed for a given material is thus defined by a set of four parameters $\theta = \{A, p, \xi, q\}$ adjusted on the desired material properties. In this work, r_0 is not considered as an adjustable parameter (*i.e.* fixed value), and the cutoff extremities $[r_{\rm cut}^{\rm s}, r_{\rm cut}^{\rm e}]$ lie between the two neighboring shells chosen at the potential development stage.

Table 1: Nominal parameters for Dufresne's and WM1 SMA potentials, reproduced from refs. [32, 35]. A and ξ are given in eV, and r_0 is in Å. $r_{\rm cut}$ column gives the atomic neighboring shells between which the cutoff interval is fixed.

	A	p	ξ	q	r_0	$r_{\rm cut}$
Duf.	0.269	7.376	2.693	2.492	3.17	$2^{\rm nd} - 3^{\rm rd}$
WM1	0.17936	9.3	2.20142	2.1	3.17	$6^{\rm th} - 7^{\rm th}$

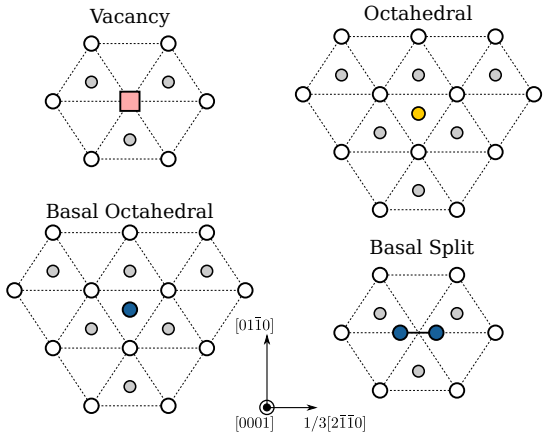

Figure 1: Projection in the basal plane of the vacancy defect and of several configurations of SIA defects. White spheres: bulk Zr atoms at $z = 0$, gray spheres: bulk Zr atoms at $z = \frac{c}{2}$. Blue spheres: Zr atoms at $z = 0$ (BO and BS SIA configurations), and yellow sphere: Zr atom at $z = \frac{c}{4}$ (O SIA configuration).

We select here two previously developed SMA potentials for Zr: the potential developed by Dufresne *et al.* [35] and the potential by Willaime and Massobrio [32], named WM1 in the original paper and herafter. Their fitted parameters, r_0 and cutoffs interval values are reproduced in Table 1. Both were developed by fitting some Zr bulk properties at $T = 0\,\mathrm{K}$. The main differences between the two SMA potentials are their range (short and medium range respectively, *cf.* Table 1) and the crystallographic structures and properties used for the fitting procedure. Dufresne's potential is fitted for fcc Zr, from lattice parameter, cohesive energy, bulk modulus B and some points of a reference energy versus distance curve [35–38]. The WM1 potential is calibrated for hcp Zr from *ab initio* and experimental values of cohesive energy, equilibrium atomic volume and elastic constants [32]. For both potentials, defect properties of any kind were not part of the adjustment procedure and are not satisfactorily reproduced, as will be discussed later. These two imperfect potentials are chosen on purpose, to illustrate the usefulness of the combined sensitivity analysis and potential refit approach.

2.2. Target properties in α-Zr

As a nuclear fuel-cladding material, hcp Zr and its alloys are subject to neutron irradiation, which triggers the formation of vacancies and self-interstitial atoms (SIAs) defects. These small point defects then diffuse into the hcp matrix, cluster and eventually form extended defects, mainly dislocation loops of both vacancy and interstitial type [39–42]. This whole process directly affects the macroscopic properties of the Zr cladding material, leading in particular to irradiation-induced growth and creep [39, 43, 44]. In this context, several basic properties relevant for irradiation growth are picked as quantities of interest (QOIs); their sensitivity to the four parameters defining the SMA potential will be evaluated. More specifically, we will focus on:

- *Bulk properties*: independent elastic constants (C_{11}, C_{12}, C_{44}, C_{13} and C_{33}), Bulk modulus B, lattice constant a, c/a ratio, and cohesive energy E_c,
- *Point defect properties:* formation energies E_f of vacancy and SIAs. Three low energy SIAs configurations, as predicted by *ab initio* calculations [45–47], are retained: octahedral (O), basal octahedral (BO) and split dumbbell in the basal plane (BS)[1], see Fig. 1,
- *Plane defect properties*: stable stacking fault energies γ_SF for the intrinsic (I_1 and I_2 configurations) and extrinsic (E) faults in the basal (0001) plane, along with stacking fault energy in the prismatic $\{10\bar{1}0\}$ planes, noted PPI in the following. Configurations are detailed in Refs. [40, 42, 48].

Small point defect properties are important for early stages of clustering, diffusion properties and defect growth, while stacking faults can be present in dislocation loops lying in both prismatic and basal planes. These latter - extended - defects are the result of irradiation point defect clustering. We note finally that the listed properties are all $T = 0\,\mathrm{K}$ properties, that may require some lattice relaxations, but are in any case *deterministic* quantities, *i.e.* there is no stochasticity involved in their computation.

Molecular statics calculations are all performed with the LAMMPS code [34], using simulation boxes having 1500 atoms for point defect calculations, and having 12 atomic planes in the direction normal to the fault for stacking fault calculations. These simulation sizes where already validated in previous studies [40, 49].

3. Screening of the SMA potentials

The goal of exploring the effect of interatomic potential parameter variation on materials properties is twofold. First, it already gives some hints on the parameter-property relationships. Second, it is a mean to identify possible artefacts related to the potential implementation. Earlier model screening works [26, 27] showed indeed many outliers and non-physical property values, *e.g.* extremely negative grain boundary energies in fcc Al, even for applied parameter variations $\leq 1\%$. Such effects naturally question the validity of the subsequent sensitivity analysis. In our case, artefacts will be also observed, and we will propose a method to improve the robustness of the SMA potential implementation.

3.1. Naive model screening

To screen the two SMA potentials, we generate 200 random parameter sets $\{\theta_i\} : \ i = 1, ..., 200$, applying a 2.5 %

[1] In refs [45, 46], a crowdion out of the basal plane is also found (BC' SIA configuration), but migration pathways from this defect configuration indicate that it is likely a saddle point configuration instead of a fully metastable configuration, so it is not included in the present study.

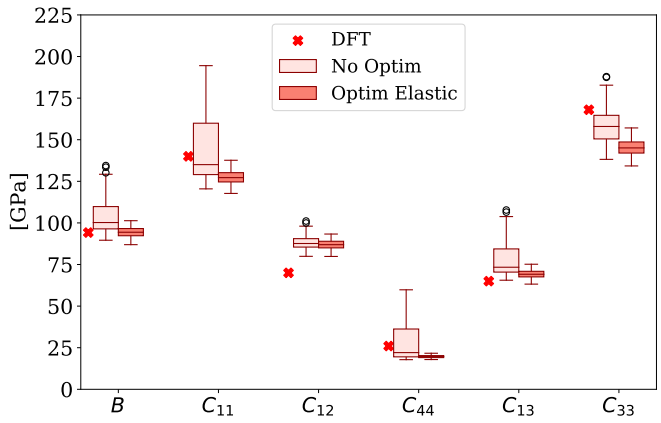

a) C_{ij}, Dufresne's potential

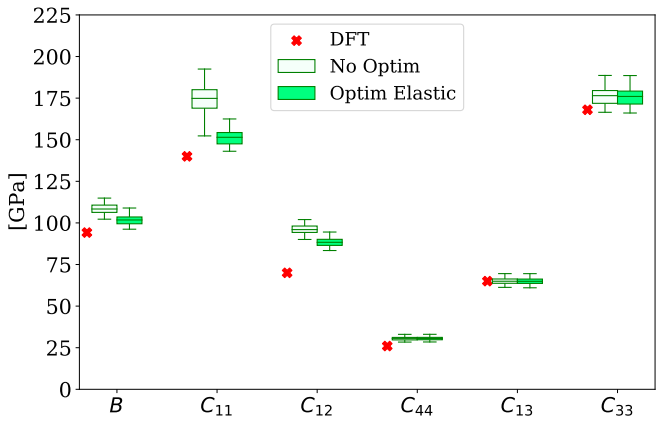

b) C_{ij}, WM1 potential

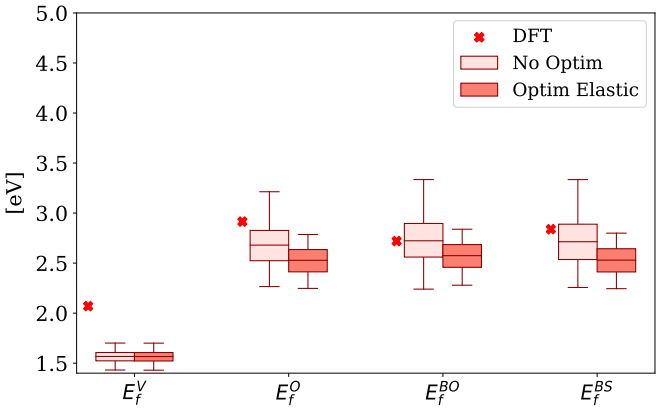

c) E_f, Dufresne's potential

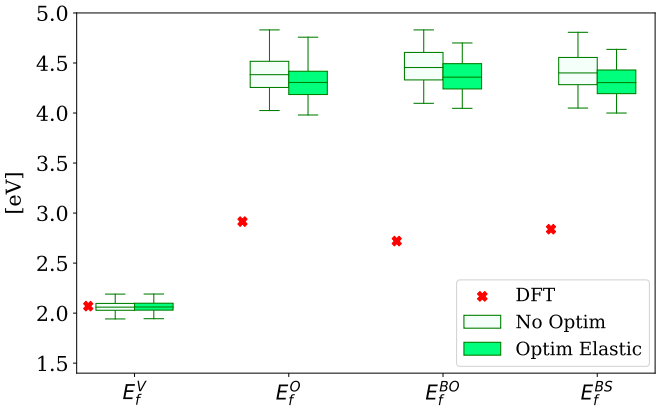

d) E_f, WM1 potential

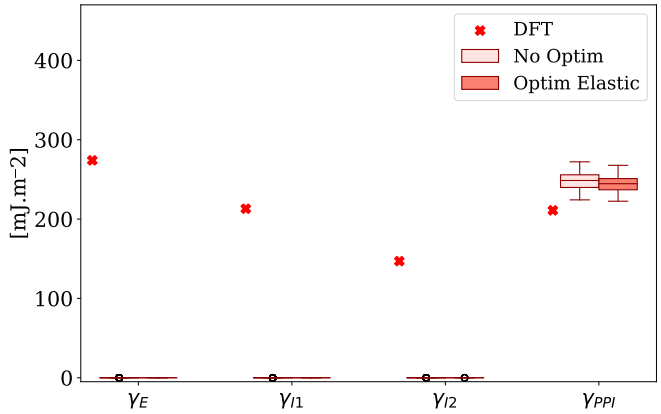

e) γ_{SF}, Dufresne's potential

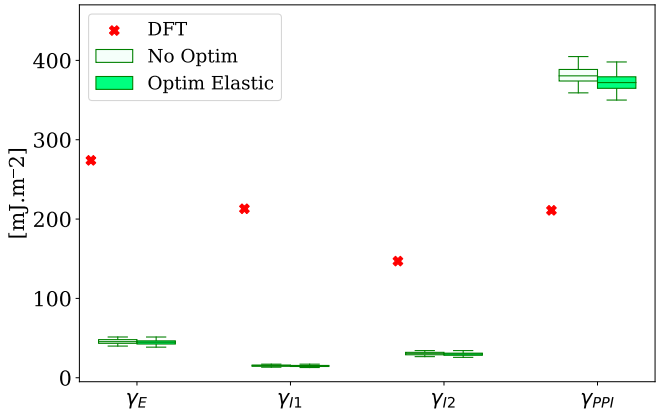

f) γ_{SF}, WM1 potential

Figure 2: Results of model screening for Dufresne's and WM1 potentials, for a parameter variation of 2.5 % around their nominal values, displayed as boxplots for (a-b) elastic constants C_{ij}, (c-d) point defect formation energies E_f for the vacancy and the O, BO and BS SIAs, and (e-f) stable stacking fault energies γ_{SF} for the I_1, I_2 and E basal faults, and for the PPI prismatic fault. The label 'No Optim' refers to naïve model screening, and the label 'Optim Elastic' to model screening performed with a search for a correct cutoff interval (see main text for details). Red crosses: reference *ab initio* values from Refs. [40, 46, 50].

variation around their nominal values (*cf.* Table 1) and assigning an uniform probability distribution for all. The cutoff interval is kept constant at its nominal value, *i.e.* $r_{\mathrm{cut}}^{\mathrm{s}}$ is located at the 2^{nd} (resp. 6^{th}) nearest neighbor position, and $r_{\mathrm{cut}}^{\mathrm{e}}$ is located at the 3^{rd} (resp. 7^{th}) nearest neighbor position of the nominal Dufresne's potential (resp. WM1 potential). Results for C_{ij}, E_f and γ_{SF} values are shown in Figs. 2(a)-(f), in the form of boxplots

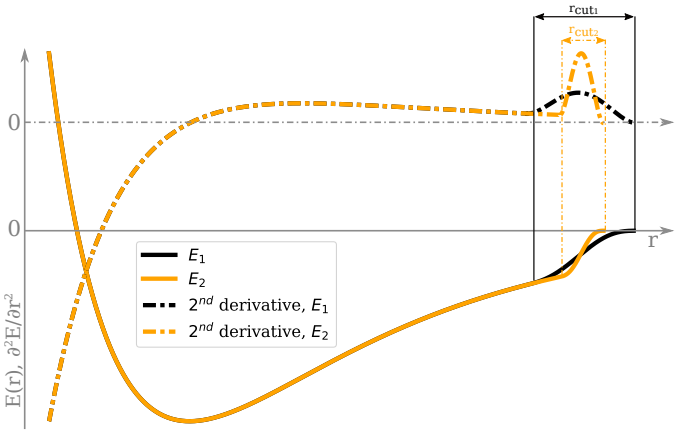

Figure 3: Effect of the cutoff interval on an total energy versus distance curve and its second derivative (Dufresne's potential and hcp structure). E_1 and E_2 correspond to the energy curves with a larger and smaller cutoff interval respectively.

for both potentials ('No optim' labels). In each box, the horizontal line inside the box indicates the median, the height of the box the interquartile range (IQR), and the whiskers extend between a distance of 1.5 times the IQR below/above the lower/upper quartile. Outliers then simply appear as points outside the whiskers.

Given the limited and symmetrically applied variation on the four SMA potential parameters (2.5 %), the observed spreading and/or skewness for a number of computed QOIs appear significant. In particular, elastic constant boxplots for the short-range Dufresne's potential (Fig. 2a) show a pronounced skewness, some outliers and a large spreading. For instance, C_{11} has values ranging from ~ 125 GPa to ~ 200 GPa. The medium range WM1 potential elastic constants (Fig. 2b) are less affected by parameter variations with a reduced skewness, but C_{11} and C_{33} still show a large scatter around their median values. For the vacancy, both potentials show a limited spreading around the median E_f value, of $\sim 0.3 - 0.4$ eV, in contrast with the SIA formation energies, for which the scatter in energy values raises $1 - 1.5$ eV and $0.7 - 1$ eV for Dufresne's and WM1 potentials, respectively (Figs. 2c and 2d). Finally, the prismatic stacking fault has a noticeable spreading of $\sim 50\,\mathrm{mJ.m^{-2}}$ for both potentials, while the spreading of basal faults is negligible (Figs. 2e and 2f). 'Artefacts' are particularly visible for elastic constants, which are partial second derivatives-related properties. As the SMA potential implementation involves a polynomial smoothing function (see Eqs. 4 and 5) whose partial derivatives differ from the SMA potential ones, the computed QOIs could be biased by keeping a fixed cutoff interval for any set of parameter θ_i.

3.2. Influence of the r_{cut} interval

To get an inkling of the effect of the cutoff interval on the computed properties, we can schematically draw the energy versus distance curve and its second derivative, with two different $[r^{\mathrm{s}}_{\mathrm{cut}}, r^{\mathrm{e}}_{\mathrm{cut}}]$ interval values. As shown in Figure 3, strong gradient/curvature zones exist in the neighborhood of the smoothing function (polynomial here, *cf.* Eq. 5). Hence, once some atoms visit these zones when computing a property - *e.g.* due to an applied deformation or to atomic relaxations around a defect - the total energy and its derivatives will strongly vary. The choice of the cutoff interval is then a sensitive task: reducing its width directly affects the curvature of the energy curve, and shifts the strong gradient zone (see Fig. 3). To improve the robustness of the potential while keeping a continuous and reasonably smooth linking of the energy to zero, one can thus intent to position the strong gradient/curvature zone in a region that is not explored by atoms in our molecular simulations. This can be done by reducing the cutoff interval up to a value that remains reasonable, so as to avoid any energy discontinuity.

(a)

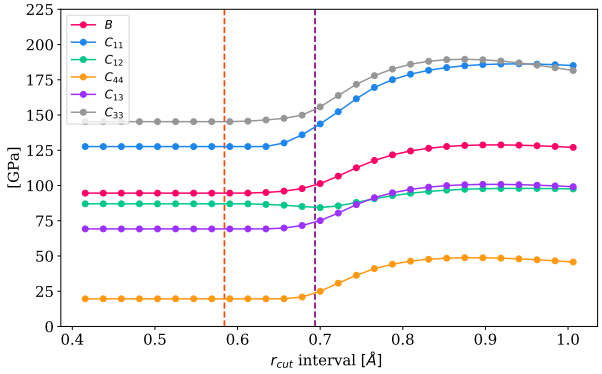

(b)

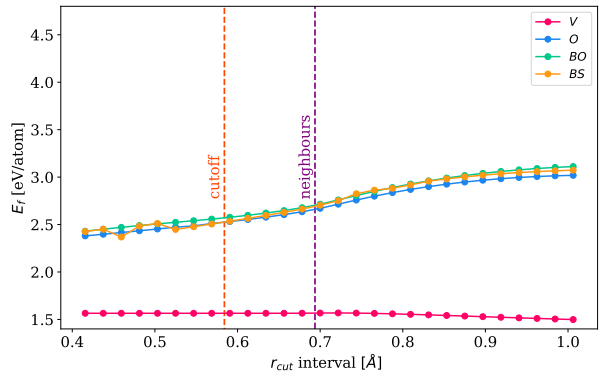

Figure 4: Bulk elastic contants B and C_{ij} (a), and formation energies E_f of the vacancy and SIA defects (b), versus length of the cutoff interval ($r^{\mathrm{e}}_{\mathrm{cut}} - r^{\mathrm{s}}_{\mathrm{cut}}$), for Dufresne's potential. The initial cutoff interval value is 40 % superior to the 2nd to 3rd nearest neighbor distance. Purple dashed line: interval for which neighbors are simultaneously crossed. Yellow dashed line: optimized cutoff interval. See main text for details.

We thus examine the evolution of α-Zr elastic constants and of the formation energies E_f of the vacancy and the various SIA defects with the length of the cutoff interval $r^{\mathrm{e}}_{\mathrm{cut}} - r^{\mathrm{s}}_{\mathrm{cut}}$, as given in Figs. 4 (a)-(b). The cutoff inter-

val is initially set to a value that is 40 % higher than the potential 2nd to 3rd nearest neighbor distance, which corresponds to a ~ 1 Å initial cutoff interval value. It is then reduced up to $\sim$ 60 % of its original length, by moving symmetrically the initial and final points $r^{\mathrm{s}}_{\mathrm{cut}}$ and $r^{\mathrm{e}}_{\mathrm{cut}}$. SMA parameters are kept at their nominal values using Dufresne's potential; similar behaviors are obtained with the WM1 potential.

As shown in Fig. 4 (a), elastic constants C_{ij} are highly dependent on the cutoff interval value, and their relationship with respect to the cutoff interval is nonlinear. For instance, an interval reduction from 1 Å to 0.64 Å leads to a decrease of more than 50 GPa for C_{11}, and reducing further the interval does not modify C_{11} anymore. By reducing the cutoff interval, all C_{ij} are seen to reach a plateau, that arises after both $r^{\mathrm{s}}_{\mathrm{cut}}$ and $r^{\mathrm{e}}_{\mathrm{cut}}$ enter within the 2nd and 3rd nearest neighbor (nn) interval. But the specific threshold interval value is different for each elastic constant. Regarding now E_f values for point defects in Fig. 4(b), while a flat curve is obtained for the vacancy, we note a sensitivity to the cutoff interval for the SIAs. Again, the variation is more pronounced up to crossing the 2nd and 3rd neighbors, which are crossed simultaneously for a cutoff interval of ~ 0.7 Å. However, a smooth variation of E_f still remains, meaning that the influence of the cutoff interval on the computed SIA energetics cannot be fully eliminated. Note also for the BS SIA some small energy jumps at small cutoff intervals, corresponding to changes in defect configurations. Thus, a too small interval is not desirable.

To summarize, observed QOIs are actually impacted by the cutoff interval value, *i.e.* properties are not only affected by the potential parameters and potential range, but also by the implementation details of the cutoff smoothing function. This is problematic for (i) MD simulations where a naive cutoff implementation could lead to uncontrolled artefacts, and (ii) for sensitivity analysis, since we aim at identifying the influence of the 'physical' SMA parameters on the QOIs with an almost transparent role of the smoothing function (*i.e.* properties must be controlled by Eqs. 2 and 3, and not by Eqs. 4 and 5).

3.3. Reduction of the cutoff bias and results

Following the above observations, we propose one optimization technique to reduce the bias induced on the QOIs by the cutoff interval. For each set of parameters θ_i, we find a cutoff interval that makes the QOIs essentially independent from it, for a given potential range (*i.e.* between 2nd and 3rd nn for Dufresne's and between the 6th and 7th nn for WM1 potential). This is done by initializing $r^{\mathrm{s}}_{\mathrm{cut}}$ (resp. $r^{\mathrm{e}}_{\mathrm{cut}}$) to a value 40 % lower (resp. higher) than that of the nominal potential, and then by systematically and symmetrically reducing the cutoff interval until the full set of C_{ij} converges to values that are independent from it. Deformations up to ± 1 % are applied to the simulation box when calculating elastic constants,[2] and a tolerance of 0.1 GPa is fixed for convergence. Note that this technique for reducing the cutoff interval bias on the QOIs is intrinsically adapted to reasonable parameter variations around their nominal values, but not to any parameter values. New screening results are represented as boxplots in Figs. 2(a)-(f) for both SMA potentials, and the corresponding model screening statistics are reported in Supplementary Materials. As before, 200 simulations are performed and the four parameters $\theta = \{A, p, \xi, q\}$ randomly vary in a 2.5 % range around their nominal values.

Overall, the skewness of all QOIs is suppressed, *i.e.* all boxplots are now symmetric around their median values. For most of the QOIs, median values are shifted as compared to the previous case where the cutoff interval was not optimized, and the spreading is significantly reduced. The spreading stays rather important for SIA formation energies, with likely some remaining effect of the cutoff interval, *cf.* the smooth energy variation seen in Fig. 4(b). The effect on the cutoff bias reduction procedure is more visible on the short-range Dufresne's potential, but is efficient and useful in both cases. The final shape of the QOIs distributions are now essentially impacted by the variation of parameters $\theta = \{A, p, \xi, q\}$, the robustness of the potential implementation is enhanced, and results of model screening, and later on sensitivity analysis, can be commented safely.

The small applied parameter variation affects differently the various C_{ij} for both SMA models: C_{44} and C_{13} display a very limited variability, in contrast to other elastic constants. SIAs formation energies show a larger spreading than the vacancy one, and the variability is similar across different configurations. Finally, basal stacking faults are almost insensitive to the (small) parameter variations. This already indicates a possible difficulty of such potentials to tune any γ_{basal} value. As an aside, we compare the nominal potentials QOIs – equal now to median values of the boxplots – to a consistent set of reference *ab initio* calculations [40, 46, 50], chosen as a reference and indicated in Fig. 2(a)-(f). While the two potentials rather well reproduce the *ab initio* elastic constants, they struggle to predict correct defect energetics (*cf.* Figs. 2(c)-(f))); in particular, WM1 potential overestimates the SIAs formation energies by 50%. Basal stacking fault energies are underestimated by both potentials, with zero values for Dufresne's potential. WM1 overestimates prismatic stacking fault and SIA formation energies.

3.4. Discussion of the robustness of the potential

The high gradient zones introduced in the SMA potentials by the smooth cutoff function can produce artefacts on the computed properties, leading to artificial and possibly non-physical results. We improved the robustness of

[2] For C_{ij} computation during the sensitivity analysis or in Table 3 the maximum applied deformation is equal to $\pm 1.10^{-4}$%

the implementation of the potentials by shifting these high gradient zones at distances that are not visited by atoms during relaxations and/or deformation. This - at least for the investigated QOIs - provides satisfying results.

Based on our observations, we can further propose some explanations for the surprising results obtained by Dhaliwal *et al.* [26, 27] in two studies, where they screen interatomic potentials applying up to 1 % variations on the nominal potential parameter values. In Ref. [27], a graphene layer is modeled with an AIREBO potential, which implementation comprises several linking functions [51] that introduce strong gradient zones. These latter are positioned at distances that can be explored by atoms if the system is distorted, *e.g.* by a defect. It is not surprising then to see strongly negative Stone-Wales defect energetics and very large spreading and number of outliers for 2D elastic constants, when performing model screening [27]. In Ref [26], the screening is performed on an EAM potential, for various bulk and defect properties of fcc Al. In contrast with our SMA case, there is no separation between a 'potential function' and a 'smoothing function': their EAM potential is defined by spline functions, with potential parameters including spline knots (parameters have no physical foundation here). Given the sensitivity of spline functions, one can easily imagine that even small parameter variations will generate strong gradient zones in the potential function, possibly leading to important artefacts in the computed properties. This is what is observed for some Al elastic constants, surface and grain boundary energies (many outliers, large spreading and/or unphysical values).

4. Identification of the most influential parameters

We now turn to the identification of the influence of potential parameters on the previously mentioned α-Zr properties (important for irradiation behavior, see section 2.2). These are zero-temperature quantities which computation is both deterministic and numerically inexpensive. Besides, the SMA potential is non-linear, so one cannot *a priori* exclude indirect effects of its parameters on the computed properties. Therefore, we select the sensitivity analysis technique based on the computation of the Sobol indices [52]. In this section, we first describe Sobol's method, and then discuss results obtained for the two SMA potentials.

4.1. Sobol indices

Sobol's sensitivity analysis is a global sensitivity analysis method that is based on variance decomposition. Its mathematical background is widely described in the literature [52], so we recall here only the necessary matter. In this subsection only, a property calculated with the SMA model is denoted as Y, with $Y = f(X_1, \ldots, X_k)$, and with the $\{X_i\}$ the set of potential parameters. The first order index that quantifies the sensitivity of Y to X_i is defined by

$$S_i = \frac{V(E[Y|X_i])}{V(Y)} = \frac{V_i}{V(Y)}, \tag{6}$$

with E denoting the expectation value. S_i estimates the part of the variance V of the property Y that is due to the variance of X_i, and expresses the *direct* effect of X_i. Sobol also introduces second order indices as

$$S_{ij} = \frac{V(E[Y|X_i, X_j]) - V_i - V_j}{V(Y)} = \frac{V_{ij}}{V(Y)}, \tag{7}$$

and higher order indices $S_{ijk}, \ldots$ defined similarly. They express the sensitivity of the variance of Y to the *interaction* of the X_i, X_j, $X_l, \ldots$, through the model. These indices are easy to interpret: their overall sum is equal to 1 and they are all positive, so the closer their value is to unity, the more the considered variable(s) – *i.e.* parameter(s) – will be influential.

A useful concept, introduced for the first time by Homma and Saltelli [53], is the so-called total sensitivity indices, that express the total sensitivity of the variance Y to a specific X_i, *i.e.* in all its forms (sensitivity to the X_i alone and sensitivity to the interactions of this variable with the other variables). The total sensitivity index S_{T_i} to the variable X_i is simply defined as the sum of all sensitivity indices relating to this variable. In the following, we will compute for each QOI only the couple (S_i, S_{T_i}) related to each potential parameter. When both indices are similar, this means that higher order indices are negligible, and their computation useless. Large differences, conversely, will indicate that the observed output is particularly affected by the interactions between potential parameters, and computation of second order indices will be performed.

4.2. Results for irradiation-relevant QOIs in α-Zr

The number of simulations required for the sensitivity analysis increases quickly with the number k of parameters (here $k = 4$). We thus use a Latin hypercube-type Sobol sequence sampling [54] to generate efficiently our set of $\theta_i = (A, p, q, \xi)_i$, with $i = 1 \ldots N$, and using the SAlib package [55]. Estimation of first and second order, along with total indices requires $N \times (2k + 2)$ simulations per QOI. Here, $N = 3750$ is used, which ensures sufficiently converged index values.

Samples are generated by considering parameter intervals of $\pm$ 2.5% around the nominal values. This is done for both potentials. It is worth pointing out that similar results in terms of sensitivity indices are obtained for both potentials by increasing the width of variation intervals up to $\pm$ 10% around the nominal parameter values. First order and total indices for all QOIs listed in subsection 2.2, and for Dufresne's and WM1 SMA potentials are given in Fig. 5. Bulk properties (elastic and lattice constants) are displayed in Figs. 5(a), and defect properties (point

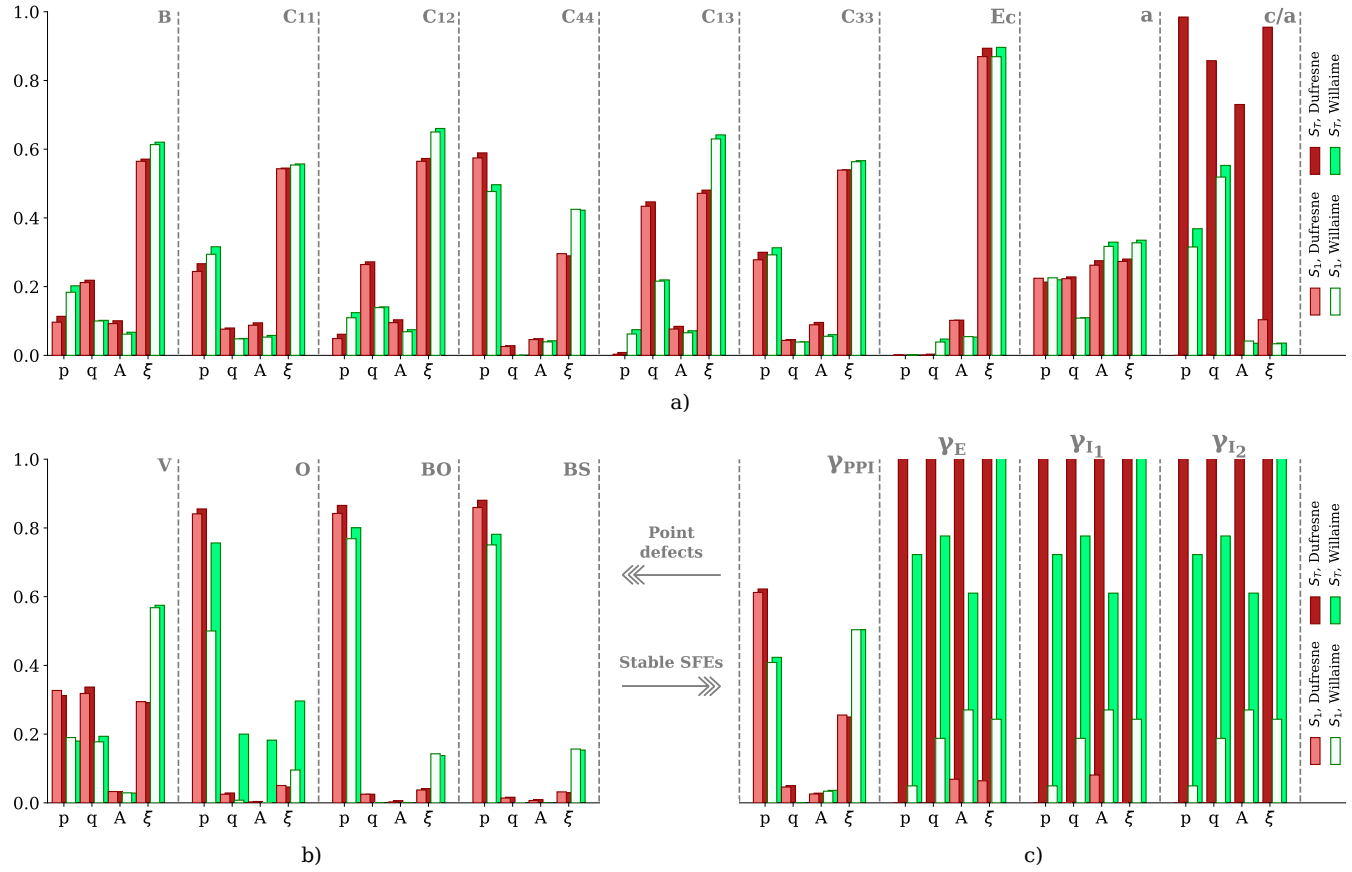

Figure 5: First order and total Sobol's sensitivity indices obtained for Dufresne's and WM1 potentials, for several QOIs: a) bulk properties (B, C_{ij}, cohesive energy and lattice parameters a and c/a ratio, b) point defect formation energies E_f (vacancy and O, BO and BS configurations of self-interstitial, and stable stacking faults energies in the prismatic (γ_{PPI}) and basal planes (γ_{E}, γ_{I_1}, γ_{I_2}).

defect formation energies and stacking faults energies) in Figs. 5(b-c).

Concerning bulk properties and for both potentials, there is a very limited difference between first order and total indices related to the four potential parameters, which means that bulk properties are essentially not affected by the interaction between the four SMA potential parameters. The only exception is the c/a ratio for Dufresne's potential, whose first order indices are way smaller than the total indices. This is due to the very short range nature of this potential: the c/a ratio get stuck in the ideal value of $\sqrt{8/3}$ when parameters are varying, so the analysis of c/a variations becomes meaningless. Besides, and again except for the c/a ratio, both potentials express the same overall sensitivity to the parameters, *i.e.* the ranking of the parameters with respect to their sensitivity indices is similar. More specifically,

- for elastic constants: ξ is the most influential parameter in all cases but one, C_{44}, where the sensitivity index for ξ just follows the one for p. The influence of A is negligible for all C_{ij}, q (resp. p) has a moderate to strong influence on B, C_{12} and C_{13} (resp. C_{11}, C_{44}, and C_{33}),
- the cohesive energy E_{c} is affected almost exclusively by ξ,
- the lattice constant a is equally moderately affected by all parameters.

The strong effect of ξ on E_{c} stems from the window of parameters used to fix both the energy scale and an equilibrium distance for the structure. Comparison of sensitivity indices for the bulk hcp structure to those calculated for fcc bulk properties in Ref. [25] indicates that the dominant role of ξ on E_{c} is retreived in the fcc case, but not the fully negligible effect of A on all elastic constants. So there exist structural specificities for sensitivity indices of bulk properties.

The case of point defects is presented in Fig. 5(b). Again, there is no significant gap between total and first order indices (except for the O SIA configuration), meaning that interactions between parameters are not important. Interestingly, for both potentials the p parameter plays the key role for all SIA configurations, while having a moderate effect on the vacancy formation energy, and (A, q, ξ) mostly do not affect SIAs energetics. This means that one could modify the SIA formation energies without modifying too much the vacancy formation energy by changing the p parameter; this is especially true for the WM1 potential. Finally, we note that differences between

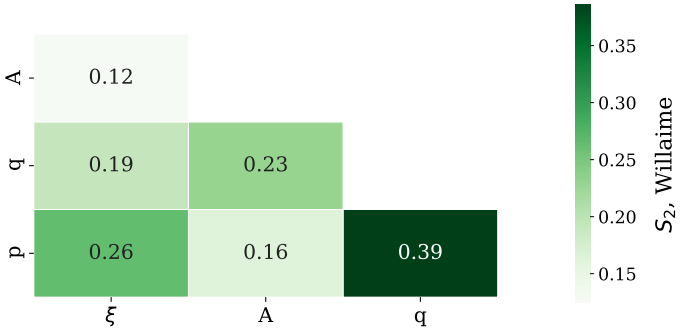

Figure 6: Second order sensitivity indices S_{ij} for the basal stacking faults, computed for the WM1 potential.

the two potentials are more pronounced for the vacancy formation energy: for Dufresne's potential S_p, S_q and S_ξ are similar, whereas S_ξ is dominant for WM1. In any case, A is not influential for the point defects E_f.

Sentivity indices for the stable stacking faults energies are displayed in Fig. 5(c). The prismatic fault shows merely equal first order and total indices with both potentials. We recall that as the position of this stacking fault is not fully determined by symmetry [50], its position was systematically determined for each set of parameter. Slight ordering differences are seen between the two interaction models: S_p is dominant for Dufresne's potential, followed by S_ξ, and negligible S_q and S_A. For WM1, S_q and S_A are also negligible, but S_p and S_ξ are similar. The case of the three basal stacking faults is more complex. All sensitivity indices obtained for the basal faults are rigorously the same: this is due to the fact that for relatively short-range potentials like the two SMA used here, the relationship $\gamma_{I_1} = \gamma_E/3 = \gamma_{I_2}/2$ must be fulfilled [56]. For Dufresne's potential, all S_i are null and the various S_{T_i} are again meaningless: this very short range potential predicts zero basal stacking fault energy whatever the potential parameters (see Fig. 2e). Results for the WM1 potential indicate important indirect effects of the potential parameters: there exist a large difference between first order and total indices.[3] To better understand interactions between parameters for this defect, we thus compute the second order indices S_{ij} (see Fig. 6). All resulting values are rather important for second order indices – S_{pq} and $S_{p\xi}$ being the highest – meaning that basal fault energies are governed by complex interactions between model parameters.

Overall, our sensitivity analysis indicates that SMA potential parameters affect differently the various QOIs considered here. The most stricking behavior is observed for point defects, where S_p appears dominant for SIAs formation energies, and not dominant for the vacancy formation energy. For most of the investigated properties, effects of parameters are reduced to their main effect, as first order indices are the most important ones. Note however that the present study is not a full global sensitivity analysis. Potential parameters are explored in a limited range around their nominal values, so generally speaking, the sensitivity indices obtained could vary when exploring the full parameter space [52]. However, given the existing similarities between indices obtained for the two SMA potentials, many observations made in this section should be rather robust against parameter variation.

[3]Sum rules of sensitivity indices are not well fulfilled due to the small variability of basal γ_{SF} (estimation problem).

5. Sensitivity indices-oriented refit of the potential

As seen in Fig. 2, none of the two SMA potentials gives correct overall defect energetics, as compared to *ab initio* predictions. Following the previous analysis, the information gained from the identification of influential parameters on QOIs can be used to reduce dimensionality for the potential refitting process. Assessing this strategy is the topic of this section, where we retain the WM1 potential as the starting point, because of the intrinsic limitations of Dufresne's model related to its very short range. We begin by detailing the chosen specifications for the new potential as well as the method followed. We then comment on the quality and efficiency of the exploration of possible solutions in the process, and end with a brief discussion of the capabilities of the re-optimized potential.

5.1. Specifications and optimization process

Recall that given the limited flexibility of SMA potentials, trying to match perfectly a too high number of quantities at the same time can be too demanding. We thus choose to test three different sets of objectives to find an improved potential for irradiation defects studies in α-Zr:

- *Set 1*: Lattice parameters, cohesion energy (a, c/a and E_c), and point defect E_f (V and SIAs);
- *Set 2*: Bulk properties (C_{ij}, a, c/a and E_c) and point defect E_f (V and SIAs);
- *Set 3*: Bulk properties (C_{ij}, a, c/a and E_c), point defect E_f (V and SIAs) and stacking faults energies γ_{SF} (prismatic PPI, basal I_1, I_2 and E).

For all sets, the objectives are equally weighted in the normalized least-squared cost functions used in the optimization process. As reference property values to be matched by the new potential, we take again a set of *ab initio* calculations performed in identical conditions, *i.e.* corresponding to a consistent set of data [40, 46, 50]. Specific values are indicated in Table 3.

Remember that for the WM1 potential, parameters A and q have little influence on most of the QOIs, p is the most influential parameter for the SIA formation energies, and ξ for the vacancy formation energy. Moderate effects of p exist on E_f^V, and of ξ on E_f^SIAs. Both p and ξ entirely determine γ_{PPI}, and their effect on the basal

faults is rather important, although largely indirect. Consequently, we keep parameters A and q at their nominal values of $A = 0.179364$ and $q = 2.1$, and follow two strategies for optimizing the potential: either we optimize only the p parameter and keep ξ at its nominal value, or we optimize the potential on both p and ξ. The former case is tested because the nominal potential was already giving good E_c, a, C_{ij} and E_f^V, and p is not the most influential parameter for these properties (except C_{44}); the latter case allows more flexibility. Note that the fact that a parameter is influential for a given property does not mean that any property value can be reached by varying this parameter. The intervals chosen for parameter variations are $p \in [7.0, 13.94]$ and $\xi \in [0.42, 3.0]$, according to a compilation of reference values [33].

For the optimization we proceed as follows. First, to speed up the optimization step,[4] polynomial chaos expansion (PCE) based surrogate models of the QOIs are developed using the Chaospy package [57], as a function of p only, and then of the couple (p, ξ). Methodological details of the PCE are presented in Supplementary Materials. An experimental plan for molecular statics simulations of the QOIs is generated by randomly drawing 5000 parameter sets in the ranges described above, and assuming a uniform probability distribution function (PDF) for the parameters of interest. Legendre polynomials of degree 4 are chosen for the PCE, since they are well suited for uniform PDFs [58]. The number of polynomial coefficients to be computed is thus 5 for the case p only, and 15 for the case (p, ξ). The convergence of the surrogate models is verified on the convergence of the first two statistical moments of all QOIs (mean and variance). For each simulation, the cutoff interval is optimised following the elastic constant-technique introduced in Section 3.3. All PCE surrogate models are provided in the Supplementary Materials. Once the surrogate models are up and running, the Python-based Pymoo package is used [59] for the various tentatives of multi-objective optimizations. The algorithm is a genetic algorithm with a modified mating and survival selection: the non-dominated sorting genetic algorithm II (NSGA-II) [60]. The convergence of the search for solutions by the NSGA-II algorithm is ensured by implementing a population size of 250 with 50 off-springs.

5.2. Explored solutions

Fig. 7 is a parallel coordinate plot representing the totality of possible solutions explored during the two optimization attempts made by varying either p or the couple (p, ξ) of parameters, and using the *Set 1* of objectives, together with objective and nominal WM1 values, and the found optima solutions for the two search cases. For most of the targeted quantities, important ranges of values are explored by the two search cases, and the objectives are well within these ranges. For the c/a ratio, however, the objective value is not included into the range visited by the algorithm: reaching the desired 1.601 *ab initio* value is clearly out of the capabilities of this SMA potential. This will be commented further in section 6. We also note that many solutions having low (resp. large) cohesive energies E_c have large (resp. low) point defect formation energies. This is connected to the definition of the formation energy, that involves the subtraction of a fraction of E_c.

Solutions explored with the *Set 2* and *3* of objectives show similar trends, and for the *Set 3* the limited exploration of the basal stacking fault energies appears connected to the limited accessible c/a values (see the parallel coordinate plots in Supp. Mater.). A close correlation exists between the c/a ratio and stacking faults in hcp materials [61], and so similarities observed during the solution searches for improving our SMA potential reflect this (see also section 6).

In general, all found optima have improved SIAs formation energies and correct/acceptable vacancy formation energy; other properties included in the cost functions are not always acceptably matched (see Fig. 2 and Supp. Mater.). As already said, the flexibility of the SMA potentials is limited, and thus the various solutions found are relative optima. Optimized potentials by varying only p have better cohesive energy and lattice parameter a than potentials optimized by varying (p, ξ), but less good point defect E_f. The overall best potential for point defects is found using the *Set 1* of objectives, and by varying the couple (p, ξ). Resulting optimized parameters are given in Table 2, including the corresponding cutoff interval $[r_{\text{cut}}^{\text{s}}, r_{\text{cut}}^{\text{e}}]$. This new potential is named ADM potential hereafter, and its performances and range of applicability are commented in the next subsection. Parameters and details of property predictions of the other optimized potentials are provided in Supplementary Materials.

Table 2: Optimized parameters of the ADM potential after multi-objective optimization on the *Set 1* of objectives, adjusting both p and ξ. Other SMA parameters are kept at their nominal values, *i.e.* $A = 0.179364$ and $q = 2.1$, and we have $r_0 = 3.17$ Å. The number of digits corresponds exactly to our potential implementation in LAMMPS.

	p	ξ	$r_{\text{cut}}^{\text{s}}$	$r_{\text{cut}}^{\text{e}}$ [Å]
ADM	7.68796909	2.29290971	6.2901771952	6.82170733956

5.3. Performances of the ADM potential

Various physical properties calculated with the newly optimized ADM potential are given in Table 3, that also contains values from the nominal WM1 potential [32], and from the two mostly used EAM potentials for α-Zr: the EAM #2 and #3 developed by Mendelev and Ackland [62]. Finally, reference *ab initio* values are given – some of them were targeted values for the ADM potential optimization and others are used to assess its transferability/extrapolation capability – and some available experimental values

[4] For one set of (A, p, q, ξ) parameters, the full sequence of QOIs calculations with LAMMPS takes 90 s, whereas the same evaluation of properties with PCE takes less than 1 s.

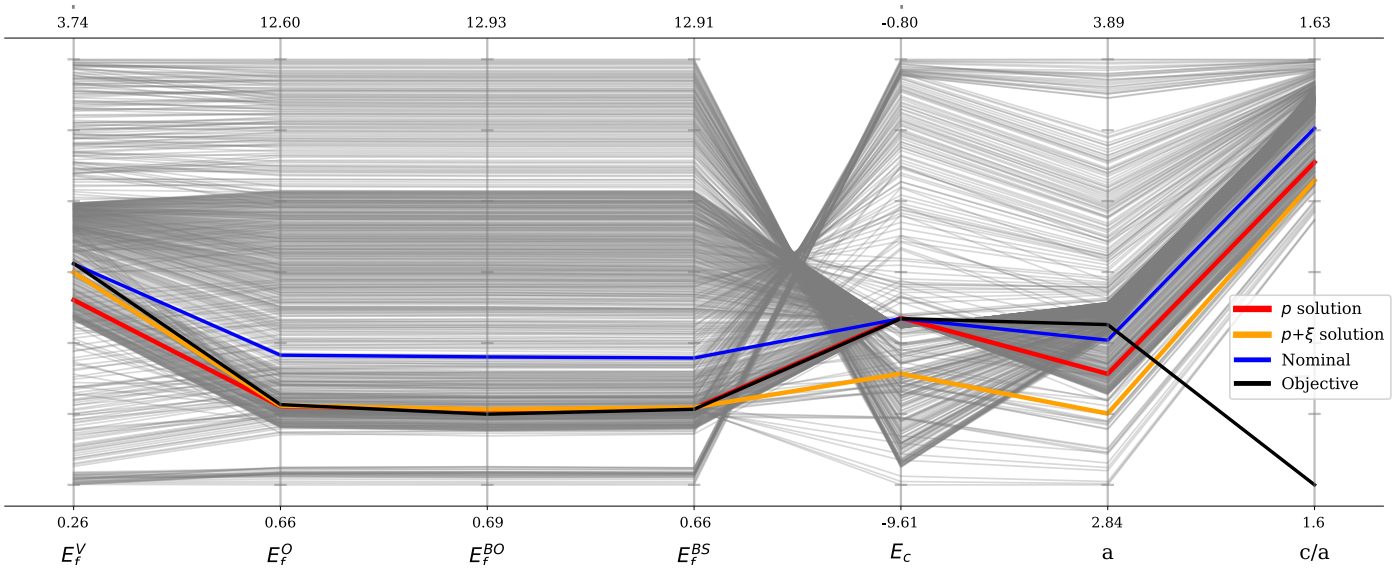

Figure 7: Parallel coordinates plot for the optimization process using the *Set 1* of objectives. Gray lines represent the possible solutions explored by the NSGA-II algorithm, the dark line represents objectives *ab initio* values, the blue line the nominal WM1 potential values, and the bold red and yellow lines the optima found by varying either p or the couple of (p, ξ) parameters.

as well. The relative difference of various interatomic potential predictions with respect to the reference *ab initio* values are provided in Fig. 8 to assist visual comparison of the potentials.

Overall, the ADM potential has improved properties as compared to the nominal WM1 potential, *i.e. the refitting procedure proposed here is operative*. Referring to *ab initio* calculations, elastic constants of the bulk hcp Zr matrix are rather well described, although not part of the *Set 1* of objectives. More specifically, B, C_{11}, C_{44} and C_{13} are very close to *ab initio* values, and C_{12} (resp. C_{33}) is a bit overestimated (resp. underestimated). Both EAM #2 and #3 potentials have similar level of agreement with respect to *ab initio* calculations (see Fig. 8). It may be noted that low-temperature experiments of elastic constants slighty differ from the *ab initio* predictions, as commonly observed for metals. Cohesive energy was part of the adjusment process, and is reasonably described as compared to *ab initio*; less accurate than the original WM1 potential, but similar to EAM #2 and #3 predictions. ADM potential predicts an hcp structure more stable than the bcc one, although the energy difference is underestimated as compared to other interaction models. Lattice constants a and c/a ratios are less accurate: a is a bit underestimated while perfectly described with all other potentials, and c/a ratio is improved as compared to the WM1 potential, but still too close to the ideal ratio. As discussed above, the target value cannot be reached by this type of SMA potential having this specific range.

The most stricking improvements of the ADM potential concern the description of point defect properties. Their formation energies were part of the cost function used in the optimization process. Considering first SIAs, the right stability ordering of defect configurations is obtained with the ADM potential, *i.e.* $E_f^{\mathrm{BO}} < E_f^{\mathrm{BS}} < E_f^{\mathrm{O}}$, and each specific value is also very close to the *ab initio* reference. This correct ordering is not retrieved by the EAM #2 potential. EAM #3 gives the correct ordering, but the BS configuration is too close in energy to the O SIA configuration. We further compare the elastic dipole tensors P_{ij} with precise values extracted from *ab initio* calculations [49]. These second rank tensors fully describe the long range interactions of point defects with strain/stress fields of various origins [67]. They were not part of the objective function, and comparing ADM values with *ab initio* reference ones is thus a first transferability check for this potential (see values in Table 4). All P_{ij} values for the SIA defects were largely overestimated by the nominal WM1 potential. ADM values are in overall very good agreement with *ab initio* results: agreement is almost perfect for both O and BO SIA configurations, and the right order of magnitude and specific ordering between P_{ij} components is predicted for the BS configuration, though P_{11} and P_{22} are closer to each other than expected from *ab initio*. Potentials EAM #2 and #3, on the other hand, both fail to predict correct P_{ij} components for the various SIA defects. In particular, P_{ij} values for the three SIA defect configurations are underestimated by the EAM #2 potential, and #3 predicts the wrong ordering of P_{ij} components for the BS defect while underestimating the magnitude of the P_{ij} for the BO SIA. So the ADM potential represent an improved description of SIAs as compared to both WM1 and the widely used EAM potentials.

Next, considering vacancies, the ADM vacancy formation energy is lower than the *ab initio* value, but less underestimated than that of the EAM #3 potential, and still higher than the lower-bound estimate from experiments [63, 64], so we consider this value as suitable. The

Table 3: Physical properties calculated with various interatomic potentials for α-Zr: WM1 [32], ADM (this work), and EAM #2 and #3 [62]. The 'Ref.' columns correspond to a consistent set of *ab initio* calculations from Refs. [40, 46, 50]. Bold values are quantities pertaining to the *Set 1* of data included in the objective function during the optimization process. Experimental values come from Refs [63–66], the vacancy migration barrier is only an isotropic estimation (*).

[GPa]	Ref.[50]	Exp.	WM1	ADM	EAM #2	EAM #3
B	94.2	97.34	98.98	93.5	100.2	99.3
C_{11}	140	155.4	142.3	131.2	149	142
C_{12}	70	67.2	89.4	84.3	75	75
C_{44}	26	36.3	28.62	23.6	44	44
C_{13}	65	64.6	63.12	64.7	76	76
C_{33}	168	172.5	175.84	151.7	168	168

[eV]	Ref.[40, 46]	Exp.	WM1	ADM	EAM #2	EAM #3
E_f^{V}	2.07	≥ 1.5	2.06	**1.84**	2.26	1.67
E_f^{BO}	2.72		4.308	**2.79**	2.87	2.79
E_f^{BS}	2.839		4.26	**2.82**	3.21	2.93
E_f^{O}	2.915		4.27	**2.96**	3.13	2.96
$E_b^{\mathrm{V_2^a}}$	0.176		0.22	0.18	0.3	-0.01
$E_b^{\mathrm{V_2^b}}$	0.094		0.23	0.21	0.31	0.07
E^c_{mig}	0.65	0.65*	0.91	0.62	1.12	0.72
$E^{\mathrm{bas}}_{\mathrm{mig}}$	0.54	-	0.88	0.61	1.03	0.63

	Ref.[50]	Exp.	WM1	ADM	EAM #2	EAM #3
E_{c} [eV]	-6.17	-6.17	-6.17	**-6.522**	-6.469	-6.635
a [Å]	3.23	3.23	3.19	**3.08**	3.22	3.23
c/a [/]	1.601	1.603	1.631	**1.628**	1.619	1.598
$\Delta E^{\mathrm{bcc}}_{\mathrm{hcp}}$ [eV/atom]	0.071		0.027	0.007	0.03	0.054

[mJ.m^{-2}]	Ref.[40]		WM1	ADM	EAM #2	EAM #3
$\gamma_{\mathrm{I_1}}$	147		9.93	20.6	55	99
$\gamma_{\mathrm{I_2}}$	213		19	41.1	110	198
γ_{E}	274		29.8	61.6	164	297
γ_{PP1}	211		367.5	299.8	357	135

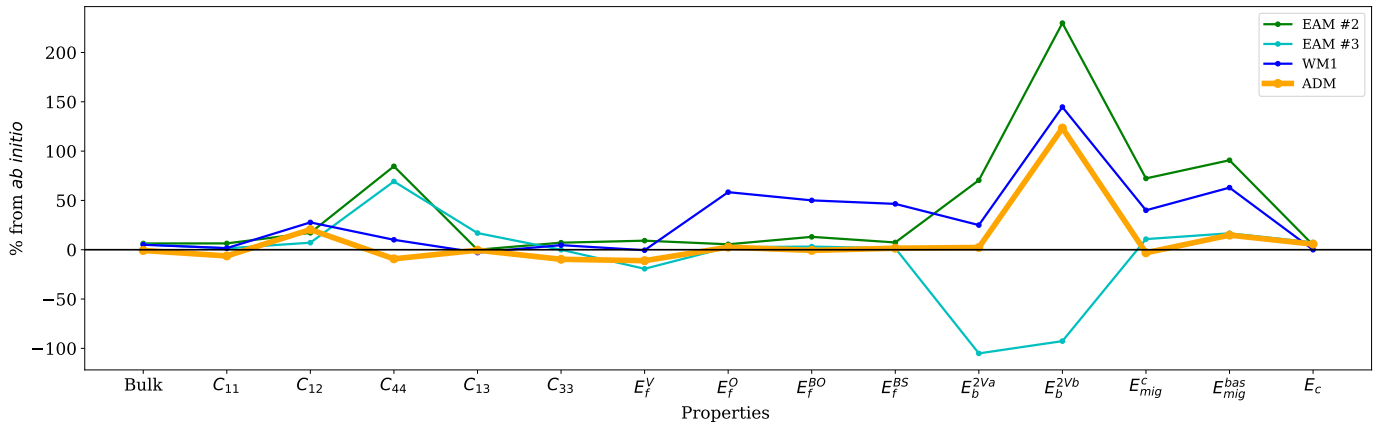

Figure 8: Relative gap between properties computed with *ab initio* calculations from Refs [40, 50] and with the original WM1 potential [32], the optimized ADM potential, and EAM#2 and #3 potentials developed by Mendelev and Ackland [62].

Table 4: Elastic dipoles in eV of the vacancy (V), of BO, O and BS SIA configurations in hcp Zr. Dipole components are obtained using the residual stress method [49]. Results are given for the ADM potential, the nominal WM1 potential [32], and the EAM #2 and EAM #3 from Ref. [62].

	V		BO		BS			O	
	P_{11}	P_{33}	P_{11}	P_{33}	P_{11}	P_{22}	P_{33}	P_{11}	P_{33}
DFT [49]	-5.14	-7.62	17.0	10.6	14.2	22.1	9.3	14.9	17.0
WM1	-4.27	-4.33	30.5	16.9	31.3	30.2	15.6	24.5	29.5
ADM	-4.73	-4.83	18.1	11.5	18.74	18.96	10.6	15.5	16.7
EAM #2	-0.65	-0.79	14.0	6.0	13.6	14.8	6.6	11.6	8.36
EAM #3	-5.43	-5.51	11.7	6.32	13.5	11.6	8.2	15.5	16.4

magnitude of the elastic dipole components is rather good although anisotropy is not sufficiently marked, similar to all tested potentials. To further check ADM potential transferability, we compute the vacancy migration energies between nearest neighbor positions in the basal plane $E^{\mathrm{bas}}_{\mathrm{mig}}$ and out of the basal plane $E^{\mathrm{c}}_{\mathrm{mig}}$ (having a component along the $\langle c \rangle$ axis). ADM values are closer to the *ab initio* ones than those of all other potentials, especially compared to those obtained with the WM1 and EAM #2 potentials. The relative order is well $E^{\mathrm{bas}}_{\mathrm{mig}} < E^{\mathrm{c}}_{mig}$, but the difference is not as large as in *ab initio* calculations. This means that the diffusion anisotropy of the vacancy will be underestimated by the ADM potential, but this comments applies to other potentials too. We also compute the binding energy between two vacancies with the usual definition $E_b^{\mathrm{V_2}} = 2E(\mathrm{V_1}) - \mathrm{E}(\mathrm{V_2}) - \mathrm{E}(\mathrm{bulk})$ [40], with a positive value implying an attractive interaction between the two vacancies. Two divacancy configurations are considered: first nearest neighbors out of the basal plane $\mathrm{V_2^a}$ and within the basal plane $\mathrm{V_2^b}$. Results for the ADM potential indicate that $E_b^{\mathrm{V_2^a}}$ almost perfectly matches the *ab initio* value, but $E_b^{\mathrm{V_2^b}}$ is too high. Nevertheless, a better prediction of the two binding energies than all other many-body potentials is achieved, in particular as compared to EAM #3 that gives no binding between vacancies, and to the binding overestimation of EAM #2. The overall attractive behavior is important for early stages of vacancy clustering under irradiation [39], and the ADM potential

is improved with this respect as compared to other potentials.

We finally comment predictions for the stacking fault energies. The prismatic γ_{PPI} of the ADM potential is somewhat acceptable and improved as compared to the original WM1 and the EAM #2 potentials, but still less accurate than the EAM #3 prediction. Basal stacking faults are the most problematic case. In addition to following the relation $\gamma_{\mathrm{I}_1} = \gamma_{\mathrm{E}}/3 = \gamma_{\mathrm{I}_2}/2$, basal stacking fault energies are way too small for the ADM potential, and definitely less accurate than those predicted by the two EAM potentials. Thus, modelling physical phenomena for which stacking fault energies matter, such as dislocation properties and glide of the $\langle a \rangle$ dislocation [50], or the stability/mobility of extended dislocation loops in both prismatic and basal planes [40, 42], are clearly beyond the capabilities of the ADM potential.

To conclude, the new ADM potential is clearly an improvement of the WM1 one, for both properties part of the objective function and others not part of it (P_{ij} of PDs and vacancy binding and migration behavior), thus showing its rather good transferability for point defect properties. It is also a good compromise between EAM #2 and #3 potentials for bulk and small point defect properties. It has been obtained after optimization of only 2 parameters over the 4 parameters of the SMA potential, thus illustrating – on this simple interaction model – the viability and usefulness of the combined approach to refit a potential: identification of influential parameters on targeted properties, development of surrogate model and multi-objective optimization process by playing with the most important potential parameters.

6. Discussion and conclusion

Although not perfect, the ADM potential is available to the community for further benchmarks and to tackle modeling studies like point defect diffusion and elasto-diffusion (recall elastic dipoles are well described), or like small defect clustering in α-Zr. This at a very reduced numerical cost, given the simplicity of this potential. On the other hand, all SMA potentials used in this work (Dufresne's, WM1 and ADM) struggle to reproduce both c/a ratio and basal stacking fault energies. The short range Dufresne's potential gives an ideal c/a ratio and zero basal stacking fault energies, whereas all medium range potentials generated in the various optimization attemps starting from the WM1 potential do explore a limited range of c/a ratio and too small basal γ_{SF} values (see Fig. 7 and Supplementary Materials). To further illustrate the effect of the potential range on both quantities, we used the ADM potential - keeping fixed its (A, p, q, ξ) values - and moved the cut-off interval between the 4^{th} and 5^{th} nearest neighbors of the hcp structure. The c/a ratio immediately decreased to the targeted ~ 1.6 value, and $\gamma_{\mathrm{I}_2} = 140\,\mathrm{mJ.m^{-2}}$, a value that is closer to the *ab initio* one. The same c/a ratio was obtained by Willaime and Massobrio for another SMA potential having similar range [32]. The potential range thus represent an *intrinsic limit* for the range of accessible c/a and basal γ_{SF} values: this is typical for potentials having no angular terms [**?**]. Note however, that shifting the potential range also modifies other physical quantities, *e.g.* both SIA formation energies and γ_{PPI} are not at all accurate after this change. Obtaining both accurate small point defect and stacking fault energies thus seems to be a difficulty for SMA interaction models. To further improve and confirm/explore the capabilities of SMA potentials for our selected QOIs, both $r^{\mathrm{s}}_{\mathrm{cut}}$ and $r^{\mathrm{e}}_{\mathrm{cut}}$ could be explicitly considered as adjustable parameters, though not having a well-defined physical meaning.

Our proposed approach to *re-optimize a potential*, using a combination of model screening, global sensitivity analysis, parameter selection/model reduction and multi-objective optimization, could theoretically be applied to the *development of an entirely new potential*. To this aim, a more global screening and sensitivity analysis – *i.e.* exploring the full parameter space and not only a reduced zone around nominal values – should be performed. However, naively applying such a process will face two difficulties. First, a wide exploration of the parameter space can occasionally lead to unsuccessful energy minimization or to nonphysical values (unstable phase, negative formation energy, etc.). Second, and this is perhaps more subtle, sensitivity indices obtained after a wide exploration of the parameter space can differ from those obtained in a reduced zone around nominal parameter values[5] [52]. Consequently, at the model reduction stage, we may eliminate parameters that are not important globally, but that become important in certain zones of the parameter space. If these regions are of interest for our potential specifications, then the multi-objective optimization process following the model reduction will not allow us to reach them. Thus, the extension of our work for the purpose of developing a new potential would require to handle these situations.

General specifications required – when screening, analysing the sensitivity and developing/refitting a classical interatomic potential for a specific physical context – can comprise of quantities more numerous and complex than the QOIs considered in this work, that are all deterministic. Stochastic quantities, typically phase transition temperatures, would require a much higher number of energy and force computations than deterministic quantities. The combined approach proposed in this work would still be applicable, but with a more systematic use of surrogate models, like *e.g.* PCEs [58, 68, 69].

Importantly, the approach could be straightforwardly applied to any empirical or semi-empirical method having typically up to tens of parameters, and for realistic sets of QOIs. This embeds not only all classes of classical inter-

[5] an inkling of this is given by Dufresne's and WM1 potentials (different range and parameter values): they have similar indices for some properties and different for others (E^{V}_f, E^{O}_f, γ_{PPI}).

atomic potentials, *e.g.* EAM [19, 20], Finnis-Sinclair [70], modified EAM [22, 23], but also approaches derived from a simplified electronic structure, either analytic bond order potentials (BOP) [71, 72], or tight-binding Hamiltonians [73–75]. Interaction models for multi-component systems can be equally considered. The case of potentials using spline functions, like some of the EAM [76, 77] and MEAM [78] potentials, deserves one more comment. Varying naively spline parameters can induce strong gradient zones that both impact sensitivity analysis results and generate not physically acceptable QOIs [26, 27]. Thus a filtering, discarding of such functions with strong gradients should be added in such cases.

The computational cost associated to Sobol's sensitivity analysis for the above cited interaction models can be important and must be discussed. Keeping the same sampling method as in section 4.2, the same $N = 3750$ and with $k = 15$ parameters, we thus have $N \times (2k + 2) = 120000$ simulations to run to compute the $\{S_i, S_{ij}, S_{T_i}\}$ for each target property. For an EAM potential, who runs in less than a minute when computing our full sequence of QOIs, we would have around 80 days of simulation time on a single processor. The sampling process can be efficiently parallelized, and thus 1 day of simulation time on 80 processors will be enough to get the results of Sobol's analysis. MEAM (or ADP) potentials would require 5-10 times that simulation time for the same calculation sequence, thus $\sim$ 5-10 days on 80 CPUs. This is typically manageable with standard laboratory/university computational resources. Finally, in the case of more computationally expensive interaction models like simplified electronic structure models and/or of models having a too high number of parameters, a quantitative sensitivity analysis will be challenging to perform, and more qualitative approaches should be adopted [79**?**]. For instance, screening and sensitivity analysis can first be performed by groups of parameters [80], thus providing a simplification of the whole study, and then a more quantitative study can be done on a reduced number of parameters. Alternatively, Morris' method [4] provides qualitative sensitivity indices. Using Morris' formula and choosing $r = 20$ trajectories, there are typically $(k+1)\times r = 320$ simulations to run. For MEAM/ADP potentials this would require roughly 2 days of computation on a single processor, and thus would be tractable for more complex interaction models like tight-binding Hamiltonians or analytical BOPs.

To summarize, model screening, sensitivity analysis, metamodeling and optimization tools can be efficiently combined to (i) provide a better understanding of the capabilities of many interaction models in predicting some targeted properties, and (ii) propose a scheme for refitting such a potential, which is based on the identification of the most influential parameters on objective quantities. We demonstrated this with a simple many-body potential, and in the context of irradiation defects in α-Zr. Despite the generally accepted idea that the accuracy of classical interatomic potentials cannot be systematically improved [1], our proposed approach gives useful guidance on the directions – rather locally in the parameter space – to follow in order to refine an existing potential. For instance, each time new *ab initio* calculations or reference data emerge, *e.g.* being more precise, or involving new relevant configurations for a specific study, a given potential can be refitted using the approach presented here, without changing the potential functional form nor adding parameters. Of course, as the flexibility of classical potentials is limited, it is likely that some properties or combinations of properties will not be perfectly reproduced. Calculations performed with such interaction models should then be accompanied by a quantification of the associated uncertainties [81–83].

Acknowledgements - Support for this work was provided by the CNRS PEPS-ANCRE PotEmQuIn research project, and by the French national funding agency through the CoCoA ANR-CE08-002-0001 grant. M.-C. Marinica is acknowledged for fruitful discussions.

Data availability - The raw/processed data required to reproduce these findings, and that are not included into supplementary materials, are available upon reasonable request to the corresponding authors.

References

[1] Y. Mishin, Machine-learning interatomic potentials for materials science, Acta Mater. 214 (2021) 1–48. arXiv:2102.06163, doi:10.1016/j.actamat.2021.116980.

[2] V. Yamakov, D. Wolf, S. R. Phillpot, A. K. Mukherjee, H. Gleiter, Deformation-mechanism map for nanocrystalline metals by molecular-dynamics simulations, Nat. Mater. 3 (2004) 43–47. doi:doi:10.1038/nmat1035.

[3] C. Dai, P. Saidi, M. Topping, L. K. Béland, Z. Yao, M. R. Daymond, A mechanism for basal vacancy loop formation in zirconium, Scr. Mater. 172 (2019) 72 – 76. doi:https://doi.org/10.1016/j.scriptamat.2019.07.006.

[4] Z. Wu, W. A. Curtin, Mechanism and energetics of $< c + a >$ dislocation cross-slip in hcp metals, Proceedings of the National Academy of Sciences 113 (40) (2016) 11137–11142. arXiv:https://www.pnas.org/content/113/40/11137.full.pdf, doi:10.1073/pnas.1603966113.

[5] D. R. Mason, S. Das, P. M. Derlet, S. L. Dudarev, A. J. London, H. Yu, N. W. Phillips, D. Yang, K. Mizohata, R. Xu, F. Hofmann, Observation of transient and asymptotic driven structural states of tungsten exposed to radiation, Phys. Rev. Lett. 125 (2020) 225503. doi:10.1103/PhysRevLett.125.225503.

[6] M.-C. Marinica, F. Willaime, J.-P. Crocombette, Irradiation-induced formation of nanocrystallites with $c15$ laves phase structure in bcc iron, Phys. Rev. Lett. 108 (2012) 025501. doi:10.1103/PhysRevLett.108.025501.
URL http://link.aps.org/doi/10.1103/PhysRevLett.108.025501

[7] M. Trochet, L. K. Béland, J.-F. Joly, P. Brommer, N. Mousseau, Diffusion of point defects in crystalline silicon using the kinetic activation-relaxation technique method, Phys. Rev. B 91 (2015) 224106. doi:10.1103/PhysRevB.91.224106.

[8] C. Varvenne, A. Luque, W. A. Curtin, Theory of solute strengthening for high entropy alloys, Acta Mater. 118 (2016) 164–176. doi:10.1016/j.actamat.2016.07.040.

[9] F. Maresca, W. A. Curtin, Theory of screw dislocation strengthening in random bcc alloys from dilute to "high-entropy" alloys, Acta Mater. 182 (2020) 144–162. doi:https://doi.org/10.1016/j.actamat.2019.10.007.

[10] J. Pirart, A. Front, D. Rapetti, C. Andreazza-Vignolle, P. Andreazza, C. Mottet, R. Ferrando, Reversed size-dependent stabilization of ordered nanophases, Nat. Commun. 10 (1) (2019) 1–7. doi:10.1038/s41467-019-09841-3.
URL http://dx.doi.org/10.1038/s41467-019-09841-3

[11] M. Ghazisaeidi, Alloy thermodynamics via the multi-cell monte carlo (mc)2 method, Comp. Mater. Sci. 193 (2021) 110322. doi:https://doi.org/10.1016/j.commatsci.2021.110322.

[12] S. Yin, Y. Zuo, A. Abu-Odeh, H. Zheng, X.-G. Li, J. Ding, S. P. Ong, M. Asta, R. O. Ritchie, Atomistic simulations of dislocation mobility in refractory high-entropy alloys and the effect of chemical short-range order, Nat. Comm. 12 (4873). doi:10.1038/s41467-021-25134-0.

[13] A. M. Goryaeva, J. Dérès, C. Lapointe, P. Grigorev, T. D. Swinburne, J. R. Kermode, L. Ventelon, J. Baima, M.-C. Marinica, Efficient and transferable machine learning potentials for the simulation of crystal defects in bcc fe and w, Phys. Rev. Mater. 5 (2021) 103803. doi:10.1103/PhysRevMaterials.5.103803.

[14] M. Liyanage, D. Reith, V. Eyert, W. A. Curtin, Machine learning for metallurgy v: A neural-network potential for zirconium, Phys. Rev. Mater. 6 (2022) 063804. doi:10.1103/PhysRevMaterials.6.063804.

[15] A. P. Bartók, M. C. Payne, R. Kondor, G. Csányi, Gaussian approximation potentials: The accuracy of quantum mechanics, without the electrons, Phys. Rev. Lett. 104 (2010) 136403. doi:10.1103/PhysRevLett.104.136403.

[16] J. Behler, Constructing high-dimensional neural network potentials: A tutorial review, Int. J. Quantum Chem. 115 (16) (2015) 1032–1050. doi:10.1002/qua.24890.

[17] A. V. Shapeev, Moment tensor potentials: A class of systematically improvable interatomic potentials, Multiscale Modeling & Simulation 14 (3) (2016) 1153–1173. arXiv:https://doi.org/10.1137/15M1054183, doi:10.1137/15M1054183.

[18] S. Starikov, D. Smirnova, T. Pradhan, Y. Lysogorskiy, H. Chapman, M. Mrovec, R. Drautz, Angular-dependent interatomic potential for large-scale atomistic simulation of iron: Development and comprehensive comparison with existing interatomic models, Phys. Rev. Mater. 5 (2021) 063607. doi:10.1103/PhysRevMaterials.5.063607.

[19] M. S. Daw, M. I. Baskes, Semiempirical, Quantum Mechanical Calculation of Hydrogen Embrittlement in Metals, Phys. Rev. Lett. 50 (17) (1983) 1285–1288. doi:10.1103/PhysRevLett.50.1285.
URL https://link.aps.org/doi/10.1103/PhysRevLett.50.1285

[20] M. S. Daw, M. I. Baskes, Embedded-Atom Method: Derivation and Application to Impurities, Surfaces, and other Defects in Metals, Phys. Rev. B 29 (12) (1984) 6443–6453. doi:10.1103/PhysRevB.29.6443.

[21] V. Rosato, M. Guillopé, B. Legrand, Thermodynamical and Structural Properties of FCC Transition Metals using a Simple Tight-Binding Model, Philos. Mag. A 59 (1989) 321–336.

[22] B.-J. Lee, M. I. Baskes, Second nearest-neighbor modified embedded-atom-method potential, Phys. Rev. B 62 (2000) 8564–8567. doi:10.1103/PhysRevB.62.8564.

[23] B.-J. Lee, M. I. Baskes, H. Kim, Y. K. Cho, Second nearest-neighbor modified embedded atom method potentials for bcc transition metals, Phys. Rev. B 64 (2001) 184102. doi:10.1103/PhysRevB.64.184102.

[24] A. Moore, C. Deo, M. Baskes, M. Okuniewski, D. McDowell, Understanding the uncertainty of interatomic potentials' parameters and formalism, Computational Materials Science 126 (2017) 308–320. doi:https://doi.org/10.1016/j.commatsci.2016.09.041.
URL https://www.sciencedirect.com/science/article/pii/S0927025616304906

[25] M. Trochet, F. Berthier, P. Pernot, Sensitivity analysis and uncertainty propagation for sma-tb potentials, Computational Materials Science 213 (2022) 111641. doi:https://doi.org/10.1016/j.commatsci.2022.111641.

[26] G. Dhaliwal, P. B. Nair, C. V. Singh, Uncertainty and sensitivity analysis of mechanical and thermal properties computed through embedded atom method potential, Comp. Mater. Sci. 166 (2019) 30–41. doi:https://doi.org/10.1016/j.commatsci.2019.03.060.

[27] G. Dhaliwal, P. B. Nair, C. V. Singh, Uncertainty analysis and estimation of robust airebo parameters for graphene, Carbon 142 (2019) 300–310. doi:https://doi.org/10.1016/j.carbon.2018.10.020.

[28] J. Friedel, The Physics of Metals, Cambridge University Press, 1969.

[29] F. Ducastelle, Modules élastiques des métaux de transition, J. Phys. 31 (1970) 1055–1062. doi:https://doi.org/10.1051/jphys:019700031011-120105500.

[30] R. P. Gupta, Lattice relaxation at a metal surface, Phys. Rev. B 23 (12) (1981) 6265–6270. doi:10.1103/PhysRevB.23.6265.
URL https://link.aps.org/doi/10.1103/PhysRevB.23.6265

[31] D. Tomanek, A. A. Aligia, C. A. Balseiro, Calculation of elastic strain and electronic effects on surface segregation, Phys. Rev. B 32 (8) (1985) 5051–5056. doi:10.1103/PhysRevB.32.5051.

[32] F. Willaime, C. Massobrio, Development of an N-Body Interatomic Potential for HCP and BCC Zirconium, Phys. Rev. B 43 (14) (1991) 11653–11665. doi:10.1103/PhysRevB.43.11653.

[33] F. Cleri, V. Rosato, Tight-binding potentials for transition metals and alloys, Phys. Rev. B 48 (1) (1993) 22–33. doi:10.1103/PhysRevB.48.22.

[34] S. Plimpton, Fast Parallel Algorithms for Short-Range Molecular Dynamics, J. Comput. Phys. 117 (1) (1995) 1–19. doi:http://dx.doi.org/10.1006/jcph.1995.1039.

[35] A. Dufresne, F. Ribeiro, G. Tréglia, How to derive tight-binding spd potentials? Application to zirconium, J. Phys. Condens. Matter 27 (33). doi:10.1088/0953-8984/27/33/336301.

[36] C. Kittel, Solid State Physics, 8th ed. (2005). arXiv:arXiv:1011.1669v3.

[37] G. Simmons, H. Wang, Single Crystal Elastic Constants and Calculated Aggregate Properties. A Handbook, 1971.

[38] P. Vinet, J. Ferrante, J. R. Smith, J. H. Rose, A universal equation of state for solids, J. Phys. C Solid State Phys. 19 (20) (1986) L467—-L473. doi:10.1088/0022-3719/19/20/001.
URL https://doi.org/10.1088/0022-3719/19/20/001

[39] F. Onimus, J. L. Béchade, 4.01 - radiation effects in zirconium alloys, in: E. in Chief: Rudy J.M. Konings (Ed.), Comprehensive Nuclear Materials, Elsevier, Oxford, 2012, pp. 1 – 31. doi:http://dx.doi.org/10.1016/B978-0-08-056033-5.00064-1.

[40] C. Varvenne, O. Mackain, E. Clouet, Vacancy clustering in zirconium: An atomic-scale study, Acta Mater. 78 (2014) 65–77. arXiv:1407.5154, doi:10.1016/j.actamat.2014.06.012.
URL http://dx.doi.org/10.1016/j.actamat.2014.06.012

[41] B. Christiaen, C. Domain, L. Thuinet, A. Ambard, A. Legris, A new scenario for $< c >$-vacancy loop formation in zirconium based on atomic-scale modeling, Acta Mater. 179 (2019) 93 – 106. doi:https://doi.org/10.1016/j.actamat.2019.07.030.

[42] C. Dai, C. Varvenne, P. Saidi, Z. Yao, M. R. Daymond, L. K. Béland, Stability of vacancy and interstitial dislocation loops in α-zirconium: atomistic calculations and continuum modelling, J. Nucl. Mater. 554 (2021) 153059. doi:10.1016/j.jnucmat.2021.153059.
URL https://doi.org/10.1016/j.jnucmat.2021.153059

[43] D. Northwood, V. Fidleris, R. Gilbert, G. J. C. Carpenter, Dislocation loop generation and irradiation growth in a zirconium single crystal, J. Nucl. Mater. 61 (2) (1976) 123 – 130. doi:https://doi.org/10.1016/0022-3115(76)90076-3.

[44] G. Carpenter, R. Zee, A. Rogerson, Irradiation growth of zirconium single crystals: A review, J. Nucl. Mater. 159 (0) (1988) 86 – 100. doi:http://dx.doi.org/10.1016/0022-3115(88)90087-6.

[45] G. Vérité, C. Domain, C.-C. Fu, P. Gasca, A. Legris, F. Willaime, Self-interstitial defects in hexagonal close packed metals revisited: Evidence for low-symmetry configurations in {T}i, {Z}r, and {H}f, Phys. Rev. B 87 (2013) 134108. doi:10.1103/PhysRevB.87.134108.

[46] C. Varvenne, F. Bruneval, M.-C. Marinica, E. Clouet, Point

defect modeling in materials: coupling ab initio and elasticity approaches, Phys. Rev. B 88 (2013) 134102.

[47] G. D. Samolyuk, S. I. Golubov, Y. N. Osetsky, R. Stoller, Self-interstitial configurations in hcp zr: a first principles analysis, Phil. Mag. Lett. 93 (2) (2013) 93–100. doi:10.1080/09500839.2012.745653.

[48] D. Rodney, L. Ventelon, E. Clouet, L. Pizzagalli, F. Willaime, Ab initio modeling of dislocation core properties in metals and semiconductors, Acta Mater. 124 (2017) 633 – 659. doi:http://dx.doi.org/10.1016/j.actamat.2016.09.049.

[49] C. Varvenne, E. Clouet, Elastic dipoles of point defects from atomistic simulations, Phys. Rev. B 96 (22) (2017) 224103. doi:10.1103/PhysRevB.96.224103.

[50] E. Clouet, Screw dislocation in zirconium: An \textit{ab initio} study, Phys. Rev. B 86 (14) (2012) 144104. doi:10.1103/PhysRevB.86.144104.
URL http://link.aps.org/doi/10.1103/PhysRevB.86.144104

[51] D. W. Brenner, O. A. Shenderova, J. A. Harrison, S. J. Stuart, B. Ni, S. B. Sinnott, A second-generation reactive empirical bond order (rebo) potential energy expression for hydrocarbons, J. Phys.: Condens. Matter 14 (4) (2002) 783. doi:10.1088/0953-8984/14/4/312.

[52] A. . Saltelli, K. Chan, E. M. Scott, Sensitivity Analysis, John Wiley & Sons, Ltd., 2008.

[53] T. Homma, A. Saltelli, Importance measures in global sensitivity analysis of nonlinear models, Reliab. Eng. Syst. Saf. 52 (1) (1996) 1–17. doi:10.1016/0951-8320(96)00002-6.
URL http://www.sciencedirect.com/science/article/pii/0951832096000026

[54] I. Sobol, On the distribution of points in a cube and the approximate evaluation of integrals, USSR Computational Mathematics and Mathematical Physics 7 (4) (1967) 86–112. doi:https://doi.org/10.1016/0041-5553(67)90144-9.

[55] J. Herman, W. Usher, Salib: An open-source python library for sensitivity analysis, Journal of Open Source Software 2 (9) (2017) 97. doi:10.21105/joss.00097.

[56] J. P. Hirth, J. Lothe, Theory of Dislocations, 2nd Edition, Wiley, New York, 1982.

[57] J. Feinberg, H. P. Langtangen, Chaospy: An open source tool for designing methods of uncertainty quantification, J. Comput. Sci. 11 (2015) 46–57. doi:https://doi.org/10.1016/j.jocs.2015.08.008.

[58] R. Ghanem, P. D. Spanos, Polynomial Chaos in Stochastic Finite Elements, J. Appl. Mech. 57 (1) (1990) 197. doi:10.1115/1.2888303.
URL http://appliedmechanics.asmedigitalcollection.asme.org/article.aspx?articleid=1409982

[59] J. Blank, K. Deb, pymoo: Multi-Objective Optimization in Python, IEEE Access 8 (2020) 89497–89509.

[60] K. Deb, A. Pratap, S. Agarwal, T. Meyarivan, A fast and elitist multiobjective genetic algorithm: NSGA-II, IEEE Trans. Evol. Comput. 6 (2) (2002) 182–197. doi:10.1109/4235.996017.

[61] B. Legrand, Relations entre la Structure Électronique et la Facilité de Glissement dans les Métaux Hexagonaux Compacts, Philos. Mag. B 49 (2) (1984) 171–184. doi:10.1080/13642818408227636.

[62] M. I. Mendelev, G. J. Ackland, Development of an Interatomic Potential for the Simulation of Phase Transformations in Zirconium, Philos. Mag. Lett. 87 (2007) 349–359. doi:10.1080/09500830701191393.

[63] G. Hood, Diffusion and vacancy properties of α-zr, J. Nucl. Mater. 139 (3) (1986) 179 – 184. doi:http://dx.doi.org/10.1016/0022-3115(86)90170-4.

[64] G. Hood, R. Schultz, J. Jackman, The recovery of single crystal α-zr from low temperature electron irradiation — a positron annihilation spectroscopy study, J. Nucl. Mater. 126 (1) (1984) 79 – 82. doi:http://dx.doi.org/10.1016/0022-3115(84)90536-1.

[65] S. Buckley, R. Bullough, M. Hayns, The direct observation of irradiation damage in zirconium and its alloys, J. Nucl. Mater. 89 (2–3) (1980) 283 – 295. doi:http://dx.doi.org/10.1016/0022-3115(80)90061-6.

[66] E. S. Fisher, C. J. Renken, Single-crystal elastic moduli and the hcp $\rightarrow$ bcc transformation in Ti, Zr, and Hf, Phys. Rev. 135 (2A) (1964) A482. doi:10.1103/PhysRev.135.A482.
URL https://journals.aps.org/pr/abstract/10.1103/PhysRev.135.A482

[67] E. Clouet, C. Varvenne, T. Jourdan, Elastic modeling of point-defects and their interaction, Comp. Mat. Sci. 147 (2018) 49–63. doi:https://doi.org/10.1016/j.commatsci.2018.01.053.

[68] N. Wiener, The Homogenous Chaos, Am. J. Math. 60 (4) (1938) 897–936. doi:10.2307/2371268.
URL https://pdfs.semanticscholar.org/21f9/b472fd25dcd75943d5da7f344cf23cfacabf.pdf

[69] P. Malliavin, Stochastic Analysis, Springer, 1997. arXiv:arXiv:1011.1669v3, doi:10.1007/978-3-642-25847-3.
URL http://link.springer.com/10.1007/978-3-642-25847-3

[70] M. W. Finnis, J. E. Sinclair, A Simple Empirical {N}-Body Potential for Transition Metals, Philos. Mag. A 50 (1984) 45–56.

[71] D. G. Pettifor, I. I. Oleinik, Analytic bond-order potentials beyond tersoff-brenner. i. theory, Phys. Rev. B 59 (1999) 8487–8499. doi:10.1103/PhysRevB.59.8487.

[72] M. Cak, T. Hammerschmidt, J. Rogal, V. Vitek, R. Drautz, Analytic bond-order potentials for the bcc refractory metals Nb, Ta, Mo and w, J. Phys.: Condens. Matter 26 (19) (2014) 195501. doi:10.1088/0953-8984/26/19/195501.

[73] F. Ducastelle, Order and Phase Stability in Alloys, North-Holland, Amsterdam, 1991.

[74] A. Dufresne, G. Treglia, F. Ribeiro, Tight-binding n-moment potential for zirconium hydride atomistic modeling, Metall. Res. Technol. 112 (2015) 102. doi:10.1051/metal/2014046.

[75] P. Eyméoud, F. Ribeiro, A. Charaf-Eddin, R. Besson, G. Tréglia, Tight-binding modeling of interstitial ordering processes in metals: Application to zirconium hydrides, Phys. Rev. B 101 (2020) 224106. doi:10.1103/PhysRevB.101.224106.

[76] Y. Mishin, D. Farkas, M. J. Mehl, D. A. Papaconstantopoulos, Interatomic potentials for monoatomic metals from experimental data and ab initio calculations, Phys. Rev. B 59 (1999) 3393–3407.

[77] M. Wen, S. M. Whalen, R. S. Elliott, E. B. Tadmor, Interpolation effects in tabulated interatomic potentials, Modelling and Simulation in Materials Science and Engineering 23 (7) (2015) 074008. doi:10.1088/0965-0393/23/7/074008.

[78] R. G. Hennig, T. J. Lenosky, D. R. Trinkle, S. P. Rudin, J. W. Wilkins, Classical potential describes martensitic phase transformations between the α, β, and ω titanium phases, Phys. Rev. B 78 (2008) 054121. doi:10.1103/PhysRevB.78.054121.

[79] S. T. Etienne de Rocquigny, Nicolas Devictor, Uncertainty in Industrial Practice: A guide to Quantitative Uncertainty Management, Wiley, 2008.

[80] G. S. Watson, A study of the group screening method, Technometrics 3 (3) (1961) 371–388.

[81] A. Del Masto, Bulk and point defect properties in α-Zr: Uncertainty quantification on a semi-empirical potential, in: Phys. Sci. For., 2022. doi:https://doi.org/10.3390/psf2022005003.

[82] F. Cailliez, P. Pernot, Statistical approaches to forcefield calibration and prediction uncertainty in molecular simulation, J. Chem. Phys. 134 (5) (2011) 054124. doi:10.1063/1.3545069.

[83] L. Kulakova, G. Arampatzis, P. Angelikopoulos, P. Hadjidoukas, C. Papadimitriou, P. Koumoutsakos, Data driven inference for the repulsive exponent of the Lennard-Jones potential in molecular dynamics simulations, Sci. Rep. 7 (1) (2017) 16576. doi:10.1038/s41598-017-16314-4.